



HAL
open science

Determination of backscattering cross section of individual particles from cytometric measurements: a new methodology.

Lucile Duforêt-Gaurier, William Moutier, Natacha Guiselin, Melilotus Thyssen, G Dubelaar, Xavier Meriaux, Lucie Courcot, David Dessailly, Hubert Loisel

► To cite this version:

Lucile Duforêt-Gaurier, William Moutier, Natacha Guiselin, Melilotus Thyssen, G Dubelaar, et al.. Determination of backscattering cross section of individual particles from cytometric measurements: a new methodology.. Optics Express, 2015, 23 (24), pp.31510-33. 10.1364/OE.23.031510 . hal-01274882

HAL Id: hal-01274882

<https://hal.science/hal-01274882>

Submitted on 22 Dec 2023

HAL is a multi-disciplinary open access archive for the deposit and dissemination of scientific research documents, whether they are published or not. The documents may come from teaching and research institutions in France or abroad, or from public or private research centers.

L'archive ouverte pluridisciplinaire **HAL**, est destinée au dépôt et à la diffusion de documents scientifiques de niveau recherche, publiés ou non, émanant des établissements d'enseignement et de recherche français ou étrangers, des laboratoires publics ou privés.



Distributed under a Creative Commons Attribution 4.0 International License

Determination of backscattering cross section of individual particles from cytometric measurements: a new methodology

Lucile Duforêt-Gaurier,^{1,*} William Moutier,¹ Natacha Guiselin,¹
Mélilotus Thyssen,² George Dubelaar,³ Xavier Mériaux,¹ Lucie
Courcot,¹ David Dessailly,¹ and Hubert Loisel^{4,5,1}

¹Laboratoire d'Océanologie et de Géosciences (LOG), Université du Littoral Côte d'Opale (ULCO), CNRS UMR 8187, 32 avenue Foch, 62930 Wimereux, France

²Mediterranean Institute of Oceanography (MIO), Université d'Aix-Marseille (AMU), CNRS/IRD UMR 7294, Campus de Luminy, 13288 Marseille, France

³CytoBuoy b.v., Jan Steenstraat 1, 3443 GP WOERDEN, The Netherlands ⁴Institut de Recherche pour le Développement (IRD), Université de Toulouse, UPS (OMP), CNRS, UMR 5566 LEGOS, 14 avenue Edouard Belin, 31400 Toulouse, France

⁵Space Technology Institute (STI), Vietnam Academy of Science and Technology (VAST), 18 Hoang Quoc Viet, Cau Giay, Hanoi, Vietnam

*lucile.duforet@univ-littoral.fr

Abstract: A methodology is developed to derive the backscattering cross section of individual particles as measured with the CytoSense (CytoBuoy b.v., NL). This *in situ* flow cytometer detects light scatter in forward and sideward directions and fluorescence in various spectral bands for a wide range of particles. First, the weighting functions are determined for the forward and sideward detectors to take into account their instrumental response as a function of the scattering angle. The CytoSense values are converted into forward and sideward scattering cross sections. The CytoSense estimates of uniform polystyrene microspheres from 1 to 90 μm are compared with Mie computations. The mean absolute relative differences ΔE are around 33.7% and 23.9% for forward and sideward scattering, respectively. Then, a theoretical relationship is developed to convert sideward scattering into backscattering cross section, from a synthetic database of 495,900 simulations including homogeneous and multi-layered spheres. The relationship follows a power law with a coefficient of determination of 0.95. To test the methodology, a laboratory experiment is carried out on a suspension of silica beads to compare backscattering cross section as measured by the WET Labs ECO-BB9 and derived from CytoSense. Relative differences are between 35% and 60%. They are of the same order of magnitude as the instrumental variability. Differences can be partly explained by the fact that the two instruments do not measure exactly the same parameter: the cross section of individual particles for the CytoSense and the bulk cross section for the ECO-BB9.

© 2015 Optical Society of America

OCIS codes: (010.4450) Oceanic optics; (010.5620) Radiative transfer; (010.1350) Backscattering; (120.4640) Optical instruments; (120.5820) Scattering measurements; (290.5850) Scattering, particles.

References and links

1. R. W. Preisendorfer, "Hydrologic optics, Vol.1: Introduction," Springfield National Technical Information Service. Also available on CD, Office of Naval Research, (1976).
2. D. Stramski, A. Bricaud, and A. Morel, "Modeling the inherent optical properties of the ocean based on the detailed composition of the planktonic community," *Appl. Opt.* **40**(18), 2929–2945 (2001).
3. A. Morel and A. Bricaud, "Theoretical results concerning light absorption in a discrete medium, and application to specific absorption of phytoplankton," *Deep Sea Res.* **28**, 1375–1393 (1981).
4. A. Bricaud and A. Morel, "Light attenuation and scattering by phytoplanktonic cells: a theoretical modeling," *Appl. Opt.* **25**(4), 571–580 (1986).
5. Y. H. Ahn, A. Bricaud, and A. Morel, "Light backscattering efficiency and related properties of some phytoplankters," *Deep Sea Res.* **39**, 1835–1855 (1992).
6. D. Stramski and D. A. Kiefer, "Light scattering by microorganisms in the open ocean," *Prog. Oceanogr.* **28**(4), 343–383 (1991).
7. R. D. Vaillancourt, C. W. Brown, R. R. L. Guillard, and W. M. Balch, "Light backscattering properties of marine phytoplankton: relationships to cell size, chemical composition, and taxonomy," *J. Plankton. Res.* **26**(2), 191–212 (2004).
8. H. Voltin, J. F. de Haan, J. W. Hovenier, R. Schreurs, W. Vassen, A. G. Dekker, H. J. Hoogenboom, F. Charlton, and R. Wouts, "Laboratory measurements of angular distributions of light scattered by phytoplankton and silt," *Limnol. Oceanogr.* **43**, 1180–1197 (1998).
9. M. S. Quinby-Hunt, A. J. Hunt, K. Lofftus, and D. Shapiro, "Polarized-light scattering studies of marine *Chlorella*," *Limnol. Oceanogr.* **34**(8), 1587–1600 (1989).
10. O. Svensen, O. Frette, and S. R. Rune Erga, "Scattering properties of microalgae: the effect of cell size and cell wall," *Appl. Opt.* **46**(23), 5762–5769 (2007).
11. J. C. Kitchen and J.R. Zaneveld, "A three-layered sphere model of the optical properties of phytoplankton," *Limnol. Oceanogr.* **37**(8), 1680–1690 (1992).
12. A. Quirantes and A. V. Delgado, "The scattering of light by a suspension of coated spherical particles: effects of polydispersity on cross sections," *J. Phys. D: Appl. Phys.* **30**, 2123–2131 (1997).
13. W. R. Clavano, E. Boss, and L. Karp-Boss, "Inherent optical properties of non-spherical marine-like particles - from theory to observations," *Oceanogr. Mar. Biol. Ann. Rev.* **45**, 1–38 (2007).
14. A. L. Whitmire, W. S. Pegau, L. Karp-Boss, E. Boss, and T. J. Cowles, "Spectral backscattering properties of marine phytoplankton cultures," *Opt. Express* **18**(14), 15073–15093 (2010).
15. A. Cunningham and G. A. Buonaccorsi, "Narrow-angle forward light scattering from individual algal cells: implications for size and shape discrimination in flow cytometry," *J. Plankton. Res.* **14**, 223–234 (1992).
16. S. G. Ackleson and R. W. Spinrad, "Size and refractive index of individual marine particulates: a flow cytometric approach," *Appl. Opt.* **27**(7), 1270–1277 (1988).
17. R. E. Green, H. M. Sosik, R. J. Olson, and M. D. DuRand, "Flow cytometric determination of size and complex refractive index for marine particles: comparison with independent and bulk estimates," *Appl. Opt.* **42**(3), 526–540 (2003).
18. R. E. Green, H. M. Sosik, and R. J. Olson, "Contributions of phytoplankton and other particles to inherent optical properties in New England continental shelf waters," *Limnol. Oceanogr.* **48**(6), 2377–2391 (2003).
19. C. Dupouy, H. Loisel, J. Neveux, C. Moulin, S. Brown, J. Blanchot, A. Leboutteiller, and M. Landry, "Microbial absorption and backscattering coefficients from in situ and POLDER satellite during an El Niño-Southern Oscillation cold phase in the equatorial Pacific (180)," *J. Geophys. Res.* **108**(C12), 8138 (2003).
20. A. Malkassian, D. Nerini, M. A. van Dijk, M. Thyssen, C. Mante, and G. Gr'gory, "Functional analysis and classification of phytoplankton based on data from an automated flow cytometer," *Cytometry Part A* **79**(4), 263–275 (2011).
21. G. B. Dubelaar, P. J. Geerders, and R. R. Jonker, "High frequency monitoring reveals phytoplankton dynamics," *J. Environ. Monit.* **6**(12), 946–952 (2004).
22. M. I. Mishchenko, L. D. Travis, and A. A. Lacis, *Scattering, Absorption and Emission of Light of Small Particles* (Cambridge University Press, 2002).
23. M. E. Lee and M. R. Lewis, "A new method for the measurement of the optical volume scattering function in the upper ocean," *J. Atmos. Oceanic Technol.* **20**(4), 563–571 (2003).
24. M. Twardowski, X. Zhang, S. Vagle, J. Sullivan, S. Freeman, H. Czerski, Y. You, L. Bi, and G. Kattawar, "The optical volume scattering function in a surf zone inverted to derive sediment and bubble particle subpopulations," *J. Geophys. Res.* **117**, C00H17 (2012).
25. T. Oishi, "Significant relationship between the backward scattering coefficient of sea water and the scatterance at 120°," *Appl. Opt.* **29**(31), 4658–4665 (1990).
26. R. A. Maffione and D. R. Dana, "Instruments and methods for measuring the backward-scattering coefficient of ocean waters," *Appl. Opt.* **36**(24), 6057–6067 (1997).

27. E. Boss and S. Pegau, "Relationship of light scattering at an angle in the backward direction to the backscattering coefficient," *Appl. Opt.* **40**(30), 5503–5507 (2001).
28. M. Chami, E. Marken, J. J. Stamnes, G. Khomenko and G. Korotaev, "Variability of the relationship between the particulate backscattering coefficient and the volume scattering function measured at fixed angles," *J. Geophys. Res.* **111**(C05), C05013 (2006).
29. J. F. Berthon, E. Shybanov M. Lee, and G. Zibordi, "Measurements and modeling of the volume scattering function in the coastal northern adriatic sea," *Appl. Opt.* **46**(22), 5189–5203 (2007).
30. J. M. Sullivan and M. S. Twardowski, "Angular shape of the oceanic particulate volume scattering function in the backward direction," *Appl. Opt.* **48**(35), 6811–6819 (2009).
31. X. Zhang, H. Lianbo, and M. X. He, "Scattering by pure water: effect of salinity," *Opt. Express*, **17**, 5698–5710 (2009).
32. J. M. Sullivan, M. S. Twardowski, J. R. V. Zaneveld, and C. Moore, "Measuring optical backscattering in water," A. Kokhanovsky, ed. *Light Scattering Reviews 7: Radiative Transfer and Optical Properties of Atmosphere and Underlying Surface* (Springer Praxis Books, 2013), pp. 189–224.
33. V. L. Dolman, "Meerhoff Mie Program User Guide," in *Internal Report Astronomy Dept.* (Free University, 1989).
34. W. Yang, "Improved recursive algorithm for light scattering by a multilayered sphere," *Appl. Opt.* **42**(9), 1710–1720 (2003).
35. O. Pena and U. Pal, "Scattering of electromagnetic radiation by a multilayered sphere," *Comput. Phys. Commun.* **180**(11), 2348–2354 (2009).
36. D. A. Siegel, "Resource competition in a discrete environment: why are plankton distributions paradoxical?" *Limnol. Oceanogr.* **43**, 1133–1146 (1998).
37. E. Aas, "Influence of shape and structure on light scattering by marine particles," *Report of Department of Geophysics* (University of Oslo, 1984), Vol. 53.
38. S. Bernard, T. A. Probyn, and A. Quirantes, "Simulating the optical properties of phytoplankton cells using a two-layered spherical geometry," *Biogeosci. Discuss.* **6**, 1497–1563 (2009).
39. M. Thyssen, G. A. Tarran, M. V. Zubkov, R. J. Holland, G. Grgori, P.H. Burkill, and M. Denis, "The emergence of automated high frequency flow cytometry: revealing temporal and spatial phytoplankton variability," *J. Plank. Res.* **30**(3), 333–343 (2008).
40. M. I. Mishchenko, "Calculation of the amplitude matrix for a nonspherical particle in a fixed orientation," *Appl. Opt.* **39**, 1026–1031 (2000).
41. D. W. Mackowski and M. I. Mishchenko, "A multiple sphere T-matrix Fortran code for use on parallel computer clusters," *J. Quant. Spectrosc. Radiat. Transfer* **112**, 2182–2192 (2011).

1. Introduction

Seawater constituents (pure water molecules, suspended particles, dissolved substances and air bubbles) impact the propagation of light through absorption and scattering processes. Absorbing and scattering characteristics of water constituents are described by the inherent optical properties (IOPs) ([1]), that do not depend on the radiance distribution. The most fundamental IOPs are the absorption coefficient $a(\lambda)$ and the volume scattering function $\beta(\lambda)$ with λ the wavelength of the radiation. From $a(\lambda)$ and $\beta(\lambda)$, three other IOPs can be defined: the backscattering coefficient $b_b(\lambda)$, the total scattering coefficient $b(\lambda)$, and the attenuation coefficient defined as $c(\lambda) = a(\lambda) + b(\lambda)$.

Since a few years now, optical instruments, such as optical backscattering sensors (Hobilabs Hydroscat, WET Labs ECO-BB or ECO-VSF) or flow-through attenuation and absorption meter (WET Labs AC-9), are dedicated to routine *in situ* measurements of IOPs. These instruments can be deployed on a large variety of platforms at different time and space scales, relevant to the sediment or phytoplankton dynamics. However, such instruments are not able to efficiently isolate and monitor the individual effects of particles on IOPs. For this reason, the particle community is treated in bulk, and the bulk IOPs of a water body result from additive contributions of all individual constituents that absorb or scatter light [2]. Note that the contribution of the dissolved matter to the scattering signal is supposed to be negligible and is therefore omitted. The dominant ecological role of phytoplankton in both open and coastal waters and the great impact on lithogenic particles in coastal waters requires that the relative contribution of the particle community on the IOPs has to be well characterized.

Although a complete optical model incorporating each and every individual component of

seawater is a very difficult task, some previous studies furthered our understanding of how the planktonic community influences the IOPs. As radiative transfer simulations provide an alternative to direct measurements, many studies were based on Mie theory assuming particles as homogeneous spheres [2–6]. These studies modeled IOPs on a detailed composition of the phytoplanktonic community, considering also non-algal particles, as viruses and heterotrophic bacteria, and non-living particles as detritus, sediments and air bubbles. Findings showed that, the relative contribution of planktonic microorganisms to light scattering is smaller than of non-living particles as detritus and sediments. However, while the absorption, attenuation and total scattering of algal cells are correctly described using the Mie theory, direct measurements realized on the volume scattering function of algal cells showed that Mie theory is less appropriate to model the backscattering [7–10]. Whitmire et al., 2010 showed from a laboratory analysis of thirteen phytoplankton species that phytoplankton cells may backscatter light at significantly higher efficiencies than what is predicted by Mie theory. Unfortunately, bulk measurements did not allow to determine precisely the individual contribution of phytoplankton, bacteria and detritus compartments.

Radiative transfer simulations realized for heterogeneous particles as coated spheres produce higher backscattering coefficient than for homogeneous spheres [11, 12]. Kitchen and Zaneveld, 1992 showed that when heterogeneous particles are considered, it is not necessary to have a high percentage of mineral-like particles or very high concentrations of submicron particles to match the observed IOPs. Bernard et al., 2009 confirmed that algal backscattering coefficients associated with coated spheres are between 5 and 25 times higher than their homogeneous volume equivalent counterparts. Cell shape can also impact the backscattering signal, more particularly for large particles as compared to the wavelength [13]. Comparisons of computations for monodispersion of randomly oriented spheroids to the computations obtained for monodispersion of volume equivalent spheres showed a strong dependence of the biases in the IOPs on particle size and shape. Biases on IOPs for polydispersions of spheroids are greater and can be higher than a factor two when the population is enriched with large particles. All these studies based on simulations or *in situ* bulk measurements resulted in controversial results. In many papers, the authors agree that further studies are required to better characterize the impact of individual cells on IOPs [13, 14].

Flow cytometry is one of the few tools used to analyse the optical properties of individual particles. A particle can be enumerated, identified and classified by analysing the scattered signals and also the fluorescence emitted by the intracellular pigments. Few approaches were developed in the past to retrieve particles properties from cytometry [15–17]. One of the more recent methods developed by Green et al., 2003 allows estimates of size and complex refractive index (real (m_r) and imaginary part (m_i)) of particles from forward and sideward scattering, and chlorophyll fluorescence combined with Mie theory. This method was used to realize particle budgets including phytoplankton, detritus and minerals from *in situ* measurements in New England continental shelf waters [18]. They showed that the summed contributions of individual particles to phytoplankton absorption and particle scattering were close to values derived from bulk measurements. Their findings highlighted that minerals contribute an important amount in the backscattering signal and detritus have a significant contribution in summer because of their high concentration at submicron sizes. In their conclusions, the authors suggest to conduct more studies to determine how their results apply in broader conditions and for some other water types, as waters with bloom conditions, new approaches will be needed because Mie theory leads to ambiguous estimates [18]. They also tested their method by comparing results from a large variety of phytoplankton cultures with Coulter Counter estimates of cell diameter and estimates of m_r and m_i resulting from inversions (using Mie theory) of bulk measurements [17]. Comparisons showed that flow cytometric estimates of m_i were well correlated with intracellu-

lar chlorophyll concentration, whereas flow cytometric estimates of m_r were not correlated with bulk estimates but stay within the range of expected values for phytoplankton cells. Dupouy et al., 2003 showed from *in situ* measurements performed in the Equatorial Pacific using FACScan flow cytometer, that while they were able to close the budget for particulate absorption, this was not the case for the particulate backscattering coefficient [19]. Green et al., 2003 concluded that their methodology is useful for distinguishing between organic and mineral particles but the accurate determination of the real part of the refractive index using flow cytometry requires some additional information about cell shape and internal heterogeneity. They indicated clearly that there is a need for new particle approaches that overcome the limitations of Mie Theory.

In this study, we developed a new methodology to derive the backscattering cross section of individual particles from measurements conducted with the benchtop and in situ deployable flow cytometer CytoSense (CytoBuoy b. v.). Opposed to single datapoints in conventional flow cytometers the CytoSense continuously digitizes and stores the running detector outputs while a particle flows at constant velocity through the sharply focused laser beam. Additional descriptors (length, total, maximum, average, inertia, center of gravity, fill Factor, asymmetry, number of cells, time of flight) are calculated based on pulse shapes. They allow for a better classification of particles, and detection of the location of specific internal cell structures [20]. Although, the proposed approach derives only the backscattering signal and does not go further the particle characterization, it is valid for homogeneous and heterogeneous spherical particles contrary to previous methodologies deriving particle diameter and complex refractive index but assuming particles as homogeneous spheres. In a first step, weighting functions were determined for the forward and sideward detectors to take into account their instrumental response as function of the scattering angle and cytometer channel values are converted into forward or sideward scattering cross section. In a second step, a theoretical relationship is developed, based on 495, 900 radiative transfer simulations for homogeneous and heterogeneous phytoplankton cells, to convert the sideward scattering cross section as measured by CytoSense into backscattering cross section. Finally, cytometric measurements on bead suspensions have been compared to bulk measurements realized with a WET Labs ECO-BB9 backscattering sensor.

2. Flow cytometry

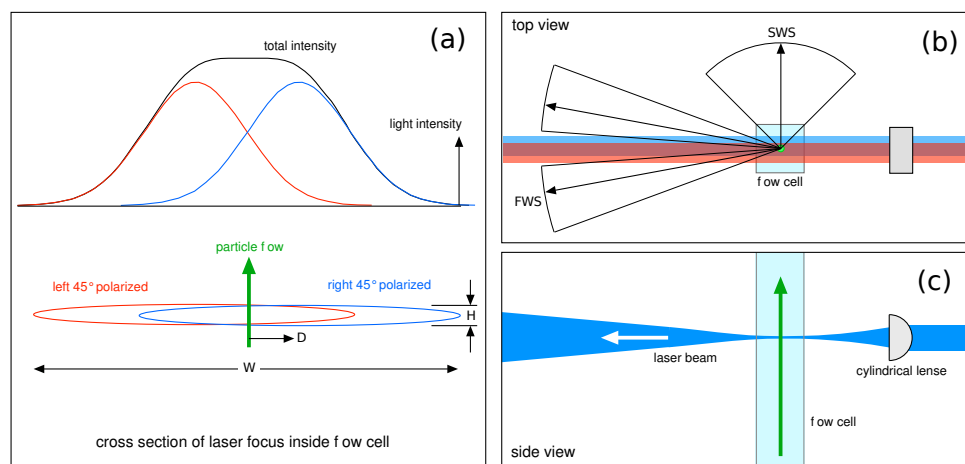


Fig. 1. CytoSense design: (a) beam shaping and light intensity distribution; (b) and (c) principle of flow cytometry.

In this study, we use the Cytosense of the PRECYM flow cytometry platform of the MIO

(<http://precym.mio.univ-amu.fr>). The CytoSense benchtop flow cytometer (CytoBuoy b.v., NL) was designed for the observation of phytoplankton cells. It measures optical properties (forward and sideward scattering, FWS and SWS, respectively) and fluorescence of their natural pigments. The practical detection level used is ca. $1\ \mu\text{m}$ (smaller for higher refractive index particles). The maximum cell size is determined by the smallest orifice in the fluid system (0.8 mm for standard CytoSenses). Digital data acquisition is initiated as each particle enters the laser beam and is terminated when the particle leaves the laser beam. The light scatter and fluorescence from each particle are collected by digitizing the data from all sensors every $0.5\ \mu\text{m}$. These digitized pulse shapes can be analyzed, giving additional information on size and internal structure. The fluorescence emitted by photosynthetic pigments in algal cells are detected at three different spectral bands. The resulting signatures are displayed as red, orange and yellow fluorescence respectively, which assist in determining the pigment type of each particle.

The sample is dosed by a peristaltic pump set at a rate of $2.47\ \mu\text{l s}^{-1}$ (selectable range $0.1 - 20\ \mu\text{l s}^{-1}$). In the flow cell, the sample stream is surrounded by the sheath fluid (saline or pure water), which fixes the final velocity of the line of particles passing through the laser (about $2\ \text{m s}^{-1}$). The flow cell has an internal fluid channel of $1 \times 1\ \text{mm}$. The material of the flat, transparent walls is quartz glass (refractive index of 1.46).

The laser is a Coherent Inc. Saphyre, 488 nm, with a power of 15 mW, a beam diameter of 0.7 mm, vertically polarized. The CytoSense beam shaping, converts the single beam in two horizontally displaced beams with polarization of $+45^\circ$ and -45° relative to the original polarisation of the laser beam. The superposition of these two Gaussian beams, with partly overlapping light distributions provides a flat light distribution over the sensing zone of the detectors. Thus, in the plane of the particle flow path, the resulting laser beam height (H) is reduced to $5\ \mu\text{m}$, and the resulting beam width (W) is about $600\ \mu\text{m}$ to encompass the suspension stream and the sheath fluid (Fig. 1(a)). The suspension stream has a width of ca. $20\text{-}200\ \mu\text{m}$ depending on the dosing rate and flows in the middle of the light distribution, where the intensity is constant. Thus, particles flowing through the intersection volume outside the middle receive the same light intensity. With this double beam solution, particles are illuminated by radiation coming from the $+45^\circ$ and -45° polarized beams. If a particle is flowing in the middle of the flow cell, the light scattered by the particle contains equal amounts of both polarization states. If a particle is flowing through the combined irradiance profile of both laser beams at some distance D away from the middle, the scattered light will contain proportionally more light from one beam than from the other one with the other polarization state. The forward scattered light (FWS) is collimated and directed onto two PIN photodiode detectors, one with a $+45^\circ$ angle polarizer in front of the photodiode and one with a -45° angle polarizer (Fig. 1(b)). In the analysis software, the signals from the two detectors are summed together to provide the forward scattering (FWS) of each particle. Their separate outputs yield the illumination ratio (and therewith the value of D) of the particle. The laser beam exiting the flow cell is absorbed in a beam stop (Fig. 1(b)). Therefore the collection solid angle of the forward scatter detectors starts at ca. 2° , going up to ca. 15° . The sideward scattered light (SWS), together with the fluorescence emission, is collected at 90° (solid angle between 45° and 135°) by a N.A.=1 objective and is directed to a series of PMT's, using a set of dichroic mirrors and band pass filters (Fig. 1(b)).

The proprietary Cytoclus software (CytoBuoy b.v., NL) was used to manually analyse the data collected by the CytoSense [21]. It enables the clustering of data points representing cells having similar optical properties, constituted by their forward and sideward scattering, and their various fluorescence signals. The clustering uses up to 10 simple mathematical signal descriptors of each available detector signal (for example, length, height, centre of gravity, asymmetry, number of humps...). The various clusters are selected manually by drawing gates in correlated bivariate scatter plots. This combines objective factors from the cytograms and

subjective considerations linked to the experience of the observer. The data of the various types of beads used could be easily discriminated in this way. A minimum detection threshold of 16mV was selected for the SWS to avoid instrumental noise and optimize the detection of calibration beads.

3. Theoretical considerations

Light scattering is produced by the presence of an object (such as a particle) with a refractive index different from that of the surrounding medium. The refractive index is expressed in complex form as $m(\lambda) = m_r(\lambda) + i m_i(\lambda)$, where λ is the wavelength of the radiation. The real part determines the phase velocity of the wave ($v(\lambda) = c/m_r(\lambda)$) with c the speed of light in a vacuum. The imaginary part represents the absorption of light as it propagates through the particle with $a_{cm}(\lambda)$ the absorption coefficient of the cellular material equal to $4\pi m_i(\lambda)/\lambda$. The angular distribution and polarization of the scattered field depend on the polarization, directional characteristics of the incident field, and on the properties of the particle as its size parameter ($x(\lambda) = \pi d/\lambda$ with d its diameter), its shape, composition, structure and orientation. The single scattering of light by an object is described by the scattering cross section $C_{sca}(\lambda)$ (units, m^2) and the phase matrix $\tilde{Z}(\lambda, \mathbf{n}_{sca}, \mathbf{n}_{inc})$ with \mathbf{n}_{inc} and \mathbf{n}_{sca} the direction of the incident and scattered radiation. The scattering cross section is defined by [22]:

$$C_{sca}(\lambda) = \frac{r^2}{I_{inc}(\lambda, \mathbf{n}_{inc})} \int_{4\pi} d\mathbf{n}_{sca} I_{sca}(\lambda, \mathbf{n}_{sca}) \quad (1)$$

with r^2 the distance from the particle. The scattered intensity I_{sca} is defined from the incident Stokes vector as follows:

$$I_{sca} = \frac{1}{r^2} (Z_{11} I_{inc} + Z_{12} Q_{inc} + Z_{13} U_{inc} + Z_{14} V_{inc}), \quad (2)$$

Note that, in Eq. (2), the spectral and directional dependency are omitted for clarity. For a spherical particle, we assume that the incident light propagates along the positive z -axis of the laboratory reference frame ($L(x, y, z)$) and that the xz -plane with $x \geq 0$ is the meridional plane of the incident beam. In this case, the Stokes vector of the scattered beam can be computed with respect to its own reference plane and the phase matrix can be written as:

$$\begin{aligned} \tilde{Z}(\lambda, \mathbf{n}_{sca}, \mathbf{n}_{inc}) &= \tilde{F}(\lambda, \theta) \tilde{L}(\phi) \\ &= \begin{pmatrix} F_{11}(\lambda, \theta) & F_{12}(\lambda, \theta) \cos 2\phi & -F_{12}(\lambda, \theta) \sin 2\phi & 0 \\ F_{12}(\lambda, \theta) & F_{22}(\lambda, \theta) \cos 2\phi & -F_{22}(\lambda, \theta) \sin 2\phi & 0 \\ 0 & F_{33}(\lambda, \theta) \sin 2\phi & F_{33}(\lambda, \theta) \cos 2\phi & F_{34}(\lambda, \theta) \\ 0 & -F_{34}(\lambda, \theta) \sin 2\phi & -F_{34}(\lambda, \theta) \cos 2\phi & F_{44}(\lambda, \theta) \end{pmatrix} \end{aligned} \quad (3)$$

with θ and ϕ the zenith and azimuthal angle of the scattered radiation and $\tilde{L}(\phi)$ the rotation matrix (see Fig. 4.6 p. 96 in [22]). The scattering matrix $\tilde{F}(\lambda, \theta)$ describing the light scattering is independent on the particle orientation and is constant with respect to the azimuth. Combining Eq. (1-3), the backscattering cross section can be written as follows:

$$C_{sca}^{bb}(\lambda) = 2\pi \int_{\pi/2}^{\pi} F_{11}(\lambda, \theta) \sin(\theta) d\theta \quad (4)$$

In marine optics, most of the commercial instruments do not measure the scattering of individual particles, so the particle community is treated in bulk. Consequently, modelling approaches have to take into account the particulate size distribution (PSD) (units, number of

particles per unit volume) that describes how particulate concentration varies with size. The ensemble-averaged quantities are defined as:

$$\langle X \rangle = \int_{d_{min}}^{d_{max}} n(d) \times X(d) dd, \quad (5)$$

with X standing for $F(\lambda, \theta)$, $C_{sca}(\lambda)$ and $C_{sca}^{bb}(\lambda)$. In theoretical modelling, the integration of the PSD over the size range is often set to unity so that radiative transfer computations are independent on the particle concentration. It results that the backscattering coefficient (b_b , units m^{-1}) and the volume scattering function (VSF, units $m^{-1}sr^{-1}$), commonly used in the formalism of marine optics, are defined from ensemble-average quantities as follows:

$$\beta(\lambda, \theta) = \langle F_{11}(\lambda, \theta) \rangle \times \frac{N}{V} \quad (6)$$

and

$$b_{bp}(\lambda) = \langle C_{sca}^{bb}(\lambda) \rangle \times \frac{N}{V}, \quad (7)$$

with N/V the particle concentration (particles per cubic meter).

4. *In situ* measurements of backscattering

In seawater, b_b and β can be partitioned into their water and particulate components: (β_w and b_{bw}) and (β_p and b_{bp}), respectively. Measurements of the VSF involve performing a very large number of measurements at discrete angles over the full angular range (from 0° to 180°). Instruments satisfying this requirement exist but are not commercially available [23, 24]. For twenty years, b_{bp} has been retrieved using a single VSF measure or a couple of VSF measures in the backward direction. For example, the WET Labs ECO-VSF measures $\beta(\theta)$ at three centroid angles (104° , 130° and 151°) and one wavelength, whereas the WET Labs ECO-BB or the HOBI Labs Hydrosat realize multi-wavelength measurements at a single angle ($\theta_s=124^\circ$ for ECO-VSF and $\theta_s=140^\circ$ for Hydrosat).

For multiple angle measurements, the VSF is simply integrated assuming a constant angular shape whatever the oceanic environments. Sullivan and Twardowski, 2009 found a remarkable consistency in shape of particulate VSF in the backward directions using a large dataset of three millions VSF measurements over oceanic and coastal waters. As only a few measurements are made, b_b is integrated over a polynomial fit to the available data.

For a single measurement of the VSF, b_b can be estimated using a conversion coefficient, named the χ factor. VSF shape analysis from Mie calculations or *in situ* measurements demonstrated that $\beta(\theta)$ at a single angle θ_s greater than 90° provides a good proxy for b_b ([25–30]):

$$b_b = 2\pi \chi(\theta_s) \beta(\theta_s) \quad (8)$$

Similar nondimensional variables ($\chi_w(\theta_s)$ and $\chi_p(\theta_s)$) can be introduced for each constituents (pure water and particles) to derive b_{bw} and b_{bp} from $\beta_w(\theta_s)$ and $\beta_p(\theta_s)$. In the vicinity of θ_s of 117° - 120° , $\chi_w(\theta_s)$, $\chi_p(\theta_s)$ and $\chi(\theta_s)$ are equal and errors in backscattering estimates are reduced to a few percent. For measurements at other angles than 117° , Boss and Pegau, 2001 suggested that the contribution of pure water (i.e., $\beta_w(\theta_s)$) to the total VSF should be removed before the conversion to yield more accurate estimates:

$$b_{bp} = 2\pi \chi_p [\beta(\theta_s) - \beta_w(\theta_s)] \quad (9)$$

Values of $\beta_w(\theta_s)$ and b_{bw} , obtained from Zhang et al., 2009, are expected to be the most accurate at this time with an accuracy around 2%. Values of $\beta_w(\theta_s)$ and b_{bw} depend on temperature and

salinity and are obtained for depolarization factor of 0.039. Sullivan et al., 2013, who examined the values of χ_p as a function of θ_s showed that χ_p has the lowest uncertainty in the range 110°-120°: mean value of χ_p is around 1.0 and the standard deviation is around 0.03%.

5. Bead method calibration

Our objective is to convert FWS and SWS magnitudes, measured by a CytoSense at 488 nm, into scattering cross sections (C_{sca}^{FWS} and C_{sca}^{SWS} , respectively). For this purpose, we calculated the forward (W_{FWS}) and sideward (W_{SWS}) weighting functions, used to describe the optical response of the two detectors, as a function of the scattering angle θ . Light is scattered from each particle through the flow cell walls onto the forward and sideward collection lens and then reaches the forward or sideward detector. The optical response of the forward detector is proportional to the area enclosed by a circle corresponding to the projection, onto the collection lense, of a cone of light, with a major half-angle of θ . Moreover, the FWS weighting function accounts for the refraction of light through the water-quartz glass interface and then through the quartz glass-air interface. Real refractive indices are $m_{HS}=1.46$ and $m_w=1.34$ for the quartz glass and water, respectively. This leads to:

$$W_{FWS}(\theta) = \pi \times [d_1 \tan(\theta) + d_2 \tan(\beta) + d_3 \tan(\gamma)]^2 \quad (10)$$

with

$$\beta = \sin^{-1} \left(\frac{m_w}{m_{HS}} \sin \theta \right) \quad (11)$$

$$\gamma = \sin^{-1}(m_w \sin \theta) \quad (12)$$

The distance d_1 is the distance from the particle to the flow cell wall (= 0.0005 m); d_2 is the thickness of the flow cell wall, (= 0.002 m); and d_3 is the distance between the cuvette to the collection lens (= 0.017 m). As the sideward scattering is too complex, a sine function was chosen to represent the weighting function as previously done by Green et al., 2003. The following relationship gave the best agreements between cytometric measurements and Mie theory:

$$W_{SWS}(\theta) = \sin \left[\frac{\pi}{2} - \sin^{-1}(m_w \sin \theta) \right] \quad (13)$$

For each detector, each weight $W(\theta)$ is normalized so the sum of all $W(\theta)$ is equal to unity.

Considering the CytoSense design, ignoring a multiplication factor, the Stokes parameters of the incident light are defined by $(I, 0, (2\alpha - 1)I, 0)$ with α the fraction of light coming from the beam with a +45° polarization. As the forward detected signal is the sum of the intensity of the two forward detectors, it is proportional to: $Z_{11}(\theta)I + (2\alpha - 1)Z_{13}(\theta)I$ with $Z_{11}(\theta)$ and $Z_{13}(\theta)$ the elements of the phase matrix (Eq. (3)). For the sideward detector with no polarizer, the detecting signal (SWS) is also proportional to $Z_{11}(\theta)I + (2\alpha - 1)Z_{13}(\theta)I$. For spherical particles, the integration of $Z_{13}(\theta) = -F_{12}(\lambda, \theta) \sin 2\phi$ over the azimuth angle is null and consequently the forward or sideward signal is only a function of $Z_{11}(\theta)I (= F_{11}(\theta)I)$, according to Eq. (3)). It means that for spherical particles, the FWS and SWS detected signals do not depend on the polarization state of the incident light.

For a given particle, the phase function is computed from Mie theory considering the particle size and refractive index. The phase function and the weighting function are computed in 0.1° increments and their product is then numerically integrated across 2°-15° (Eq. (14)) and 45°-

135° (Eq. (15)) to calculate the theoretical forward and sideward cross sections:

$$FWS_{Mie} = \sum_{\theta=2^{\circ}}^{\theta=15^{\circ}} W_{FWS}(\theta) F_{11}(\theta) \sin(\theta) d\theta \quad (14)$$

$$SWS_{Mie} = \sum_{\theta=45^{\circ}}^{\theta=135^{\circ}} W_{SWS}(\theta) F_{11}(\theta) \sin(\theta) d\theta \quad (15)$$

The upper and lower limits (2°-15°) and (45°-135°) correspond to the field of view of the forward and sideward detectors. These estimates include the refraction at exiting the quartz.

Polystyrene (PS) beads of several sizes (1.0, 1.5, 3.0, 4.5, 6.0, 10.0, 20.0, 25.0, 45.0, 75.0, 90.0 μm) (Polysciences Inc., cat. 07310-15, 17133-15, 17134-15, 17135-5, 07312-5, 17136-5, 18329-5, 07313-5, 07314-5, 24049-5, 07315-5) are used to compare the theory-based estimates (FWS_{Mie} and SWS_{Mie}) (Eqs. (14) and (15)), and the CytoSense measurements (FWS_{cyto} and SWS_{cyto}) for forward and sideward scattering. For a bead with a diameter d , the signal as measured by the CytoSense FWS_{cyto} (in numerical counts, NC) is converted into forward or sideward cross section (μm²) using a reference bead (RF):

$$FWS(d) = \frac{FWS_{Mie}(RF)}{FWS_{cyto}(RF)} \times FWS_{cyto}(d). \quad (16)$$

The same equation can be written for the sideward scattering with SWS instead of FWS. The refractive index of polystyrene is 1.20 relative to pure water at 488 nm. Beads are supposed to be non-absorbing. Images obtained from scanning electron microscopy (SEM LEO 438VP, accelerating voltage of 15 keV with a beam current of 10 pA) show that PS beads are uniform spheres. For each size samples, diameters of a hundred of beads randomly chosen were measured from micrographs. Results show that the measured mean diameter is close to the diameter indicated by the manufacturer and the coefficients of variation range between 1 and 10% according to the bead size.

For each detected particles, the CytoSense records the complete pulse shape, as opposed to single datapoints in conventional flow cytometers. By integrating the complete pulse shape, we can reconstruct the entire signal scattered by the particle in the forward and sideward directions. The integrated FWS and SWS are then reported on cytograms. Eleven clusters corresponding to the eleven samples of different bead sizes were selected from cytograms using CytoClus software. For each cluster, we calculated the mean FWS and SWS signals and their coefficients of variation. For the PRECYM CytoSense, coefficients of variations range between 1.6% and 8.4% for forward scatter and between 0.7% and 20.2% for sideward scatter. Figure 2 compares the forward and sideward scattering cross section as predicted by Mie theory and measured by the PRECYM CytoSense, as a function of the particle diameter. Microspheres of 10 μm diameter were selected as reference particles as they were in the middle of the distribution in particle size. For forward scattering, the linear regression between Mie estimates and cytometric measurements gives a coefficient of determination R² of 0.88. Absolute relative differences ΔE, between Mie and CytoSense estimates, are between 4.8% and 88.1% with a mean value of 27.9%. ΔE of 88.1% is obtained for beads with a diameter of 3 μm. If we disregarded 3 μm beads, ΔE are between 4.8% and 48.7%, and the mean value decreases (= 21.3%). For sideward scattering, ΔE are between 10.5% and 87.5% with a mean value of 41.8%. Highest ΔE are obtained for largest particles. Good agreements are observed especially in the size range of 1 to 20 μm. If we considered only particles less than 25 μm, the mean ΔE decreases from 41.8% to 20.1% for SWS. Note that mean absolute relative differences have the same order of magnitude as values previously observed by Ackleson and Spinrad, 1988 on a similar exercise realized from measurements of the Coulter EPICS V flow cytometer. The authors found mean ΔE of 16.9% for FWS and 30.1% for SWS considering beads between 1.5 and 32 μm.

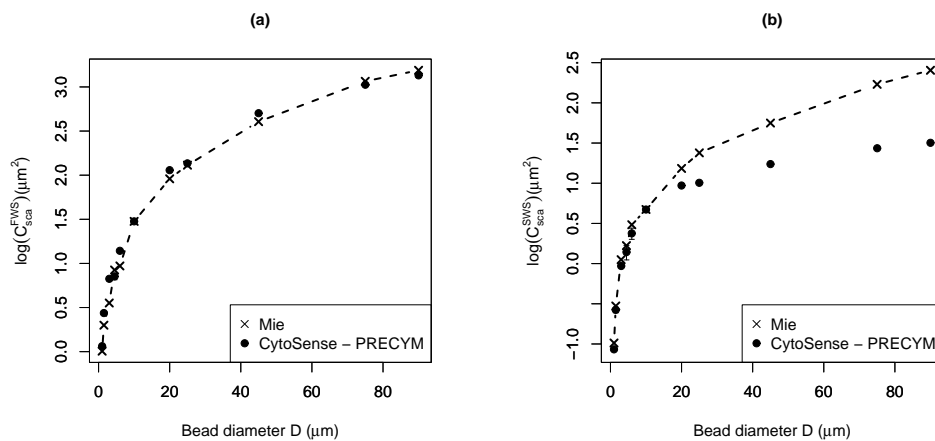


Fig. 2. Comparison of measured scattering cross sections (dots) and scattering cross sections as predicted by Mie theory (crosses) in (a) forward and (b) backward directions for the PRECYM CytoSense.

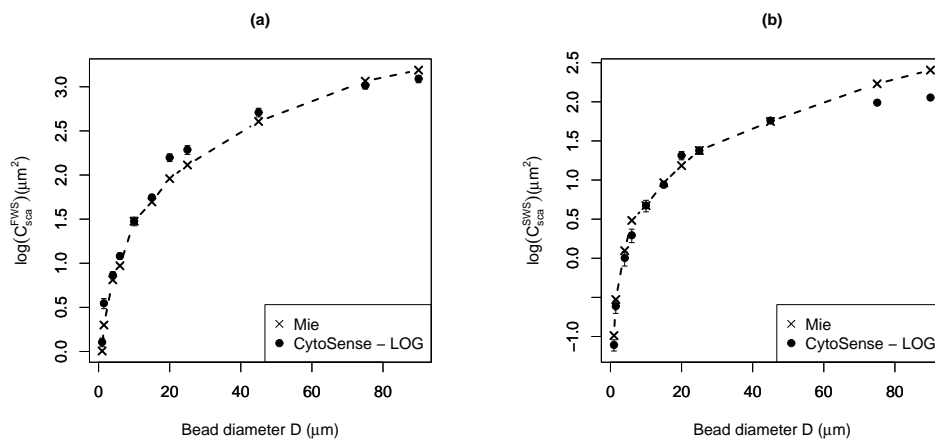


Fig. 3. Same as Fig. 2 for the LOG CytoSense.

The PRECYM CytoSense tends to underestimate the scattered for large particles, especially in the sideward direction. It is due to the saturation of the photomultipliers (PMT's) used for the detection of sideward scattering. To test this hypothesis, measurements on polystyrene beads were realized with another CytoSense belonging to the LOG laboratory (<http://log.univ-littoral.fr/>). The LOG CytoSense is quasi-identical to the PRECYM CytoSense, except that it is equipped with two different sets of photomultiplier tubes with low and high sensitivity (instead of one single PMT's set for the PRECYM CytoSense). As expected, Figure 3 shows that the signal saturation of SWS detectors is less pronounced for the LOG instrument. It results that the LOG instruments give better estimates for large particles. For FWS, ΔE range between 11% and 76% with a mean relative difference (ΔE) of 33.7%. For SWS, ΔE range between 0.2 and 55%, with a mean value of to 23.9%. For particles with diameters below 60 μm , the maximum ΔE value is equal to 35%. Over the vertical height of 5 μm the initial light distribution of the resulting laser beams remains approximately more or less Gaussian. Consequently, the assumption of Mie theory considering the spatial distribution of incident radiation as homogeneous, can be a source of errors. This point has already been discussed by Ackleson and Spinrad, 1988. As the differences between predicted and observed cross sections did not increase with particle size, Ackleson and Spinrad, 1988 concluded that errors due to Mie assumption were probably small because the horizontal dimension of the laser beam was large relative to the size of the particles. When we considered the LOG CytoSense and particles between 1 and 40 μm (no light saturation of the FWS and SWS detectors), we did not observe a increase of errors with the particle size. As microspheres are smaller than the horizontal dimension of the beam, we assume, as in Ackleson and Spinrad, 1988, that the Mie theory can be used in this calibration exercise.

6. Backscattering estimates from CytoSense

Table 1. Statistical relationship between the sideward and the backward cross sections, $C_{sca}^{bb}(488\text{nm}) = 10^B \times [C_{sca}^{SWS}(488\text{nm})]^A$, calculated from theoretical computations for homogeneous and two or three-layered spheres.

Model*	A	B	R^2
100%	1.16	-0.77	0.96
80%-20%	1.10	-0.52	0.98
70%-30%	1.12	-0.59	0.98
60%-40%	1.14	-0.62	0.98
80%-10%-10%	1.11	-0.51	0.95
80%-18.63%-1.37%	1.09	-0.51	0.87

*Percentages are the relative proportions of the cytoplasm, chloroplast and silica wall. 100% represents an homogeneous sphere.

The angular dependence of phase functions, observed from literature, seems to present a constant proportionality between the sideward scattering and the backscattering. The objective of this section is to develop a theoretical relationship to convert C_{sca}^{SWS} into C_{sca}^{bb} from radiative transfer simulations.

The Meerhoff Mie program, version 3.0, [33] and the Scattnlay algorithm [34, 35] were used to simulate the scattering and absorbing properties of homogeneous and multi-layered spheres, respectively. The Mie code is mainly used to simulate scattering properties of reference beads (polystyrene and silica beads), whereas the Scattnlay algorithm is dedicated to model

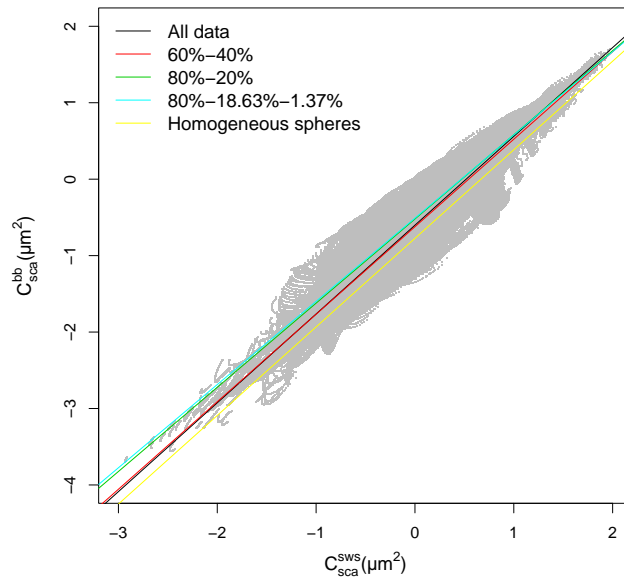


Fig. 4. Backscattering cross section as a function of sideward scattering cross section. Color lines corresponds to regression slopes performed for the whole dataset (black), homogeneous spheres (yellow), two-layered spheres (red and green) and three-layered spheres (light blue)

phytoplankton cells. The phase function is simulated, from 0° to 180° , in 0.2° increments. The 0.2° increments are required to obtain accurate numerical integrations. The theoretical phase function will be integrated later over θ to calculate theoretical sideward scattering cross section (C_{sca}^{SWS}) as measured by a CytoSense and the theoretical backscattering cross section (C_{sca}^{bb}).

In marine optics, suspended particulate matter includes particles with sizes ranging between 0.2 and $200 \mu\text{m}$ in diameter ([36]). The lower bound is an operational cutoff value between dissolved and particulate material, corresponding to the pore size of a polycarbonate membrane filter. The upper bound stands for the upper bound of particles that can still be assumed to be distributed as a continuum in operational optical measurements. Although contemporary CytoSenses and other flow cytometers can analyse smaller particles, radiative transfer simulations were limited to particles with diameters larger than $1 \mu\text{m}$ for practical reasons. Moreover, due to the saturation of PMT's, C_{sca}^{SWS} estimates are correct for particles with a diameter up to $20 \mu\text{m}$ and $40 \mu\text{m}$, for PRECYM and LOG CytoSense, respectively. Consequently, simulations are carried for diameters between 1 to $40 \mu\text{m}$.

Firstly, phytoplankton cells are considered as homogeneous spheres. Values of m_r , from 1.03 to 1.09 , corresponds to cells with a high water content. The imaginary part m_i spans from 0.001 to 0.015 with a upper limit associated with strongly absorbing bands of photosynthetic pigments ([2, 3, 12]). Secondly, the morphology of phytoplankton cells is modeled as a two or three-layered sphere. The inner layer stands for the cytoplasm, which dominates the cell volume and is considered weakly absorbing as it is mostly composed of water. For two-layered spheres, the outer layer represents the chloroplast containing highly-absorbing pigment-protein, responsible for photosynthesis. For three-layer spheres, the chloroplast is the middle layer and

the outer layer is the frustule, a silica wall. An exhaustive review of appropriate relative volume and refractive index ranges for cellular chloroplast, cytoplasm and frustule were realized by Bernard et al., 2009, from the available literature. In our computations, for the three-layered sphere model, the relative proportions of cytoplasm/chloroplast/silica wall are 80%-18.63%-1.37% and 80%-10%-10%. For the two-layered spheres model, the relative proportions of cytoplasm/chloroplast are: 80%-20%, 70%-30% and 60%-40%. The complex refractive indices of cytoplasm ($m_r(\text{cyto}) + i m_i(\text{cyto})$) and silica wall ($m_r(\text{wall}) + i m_i(\text{wall})$) are set equal to $1.02 + i 2.07E10^{-4}$ and $1.07 + i 0.0001$, respectively. Concerning the chloroplast, $m_r(\text{chloro})$ and $m_i(\text{chloro})$ are chosen so that the equivalent m_r and m_i of the phytoplankton cell are between values of m_r and m_i selected for homogeneous spheres. Volume equivalent m_r and m_i are calculated from the Gladstone-Dale relationship [37]:

$$\sum_j m_r^j V_j = m_r \sum_j V_j \quad (17)$$

where the subscript j ($=1,2$ or $1,2,3$) refers to the j -th component and V_j is the respective volume of the j -th layer. In the same way, Eq.(17) can be written for m_i . Note that $m_r(\text{chloro})$ and $m_i(\text{chloro})$ as calculated from the Gladstone-Dale formula range between published values of chloroplast refractive indices [38].

From the synthetic database made up of 495,900 computations realized at 488 nm, the relationship between C_{sca}^{SWS} and C_{sca}^{bb} is examined. Figure 4 suggests that the theoretical relationship follows a power law:

$$C_{sca}^{bb}(488nm) = 10^B \times [C_{sca}^{SWS}(488nm)]^A, \quad (18)$$

with A and B the slope and the intercept of the regression calculated from data in log space. For the whole dataset, A = 1.16 and B = -0.60, and the coefficient of determination R^2 is of 0.95. If we consider the different models independently, the regression slope varies between 1.09 and 1.16 and the intercept varies between -0.51 and -0.77 (Fig. 4 and Table 1). It shows that the model (homogeneous or heterogeneous with two or three layers) impacts the scattering of data around the mean relationship calculated over the whole dataset. As expected homogeneous particles have a smaller C_{sca}^{bb} for a given C_{sca}^{SWS} (due to the weaker intercept) confirming that homogeneous particles backscatter less than heterogeneous particles. Particle diameter, refractive index (real and imaginary part) impacts the scattering of data and their influence varies according the considered model (Figs. 5, 6, 7). For homogeneous particles, the scattering of data seems to be more impacted by the real refractive index than by the particle size. Data corresponding to particles with d ranging between [1-10[μm , [10-20[μm , [20-40] μm , are dispersed along the slope (Fig. 5(a)) (with small C_{sca}^{SWS} and C_{sca}^{bb} corresponding to small sizes), whereas data corresponding to particles with m_r between [1.03-1.05], [1.05-1.07], [1.07-1.09] are dispersed from either side of the regression (Fig. 6(a)). Similar observations can be done for the two-layered particles corresponding to the 60%-40% model. However, this is not the case, for example, for the 80%-18.63%-1.37% or 80%-20% model where data corresponding to d between 1-10 μm and 10-20 μm overlap data corresponding to different ranges of m_r and m_i (Figs. 5–7(b) and Figs. 5–7(d)). In these cases, the scattering of data results from a combination of the influence of d , m_r and m_i . Smallest R^2 values are observed for three-layered spheres with R^2 around 0.9. The refractive index greatly influences the scattering of heterogenous particles when the relative proportions of the peripheral layers is greater. It is consistent with Bernard et al., 2009's findings who showed that the real refractive index of any peripheral layer can be considered as one of the most important parameters causing variations on backscattering. For applications in a natural environment, it is obvious that C_{sca}^{SWS} will be converted into C_{sca}^{bb} using the regression performed on the whole dataset (Eq. (18), with A = 1.16 and B = -0.60) as in natural environments the morphology of particles is unknown in most cases.

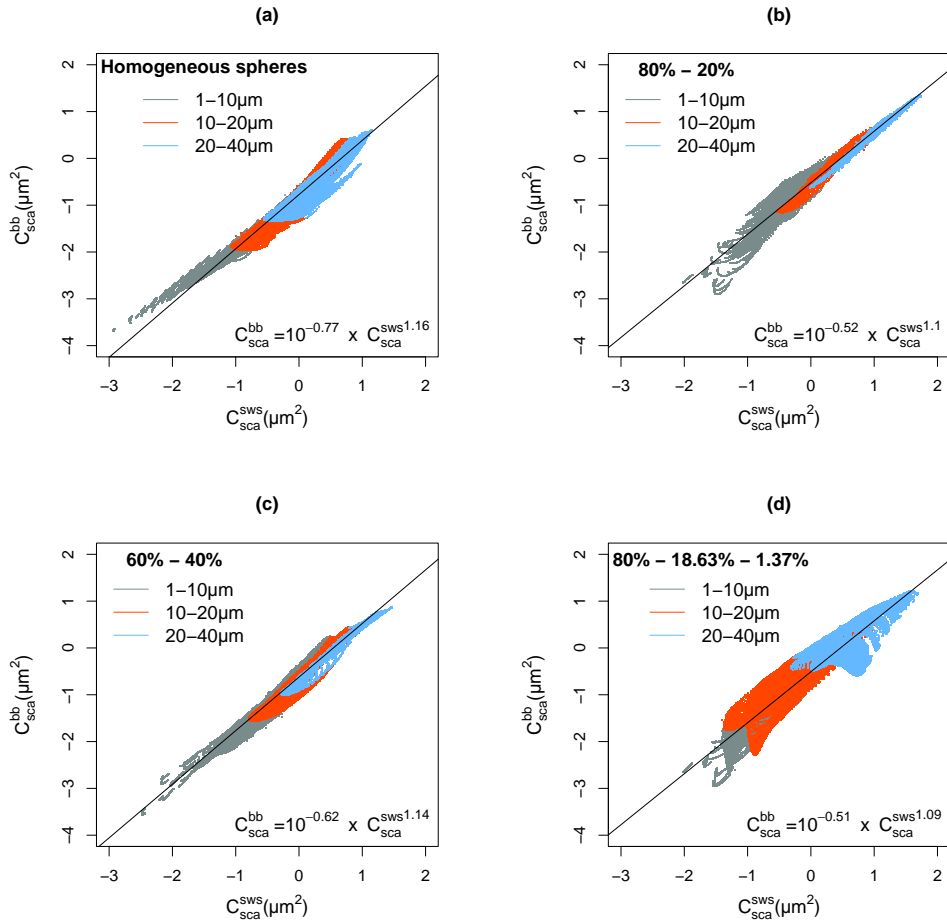


Fig. 5. Backscattering cross section as a function of sideward scattering cross section. (a) homogenous spheres (b)-(c) heterogenous spheres with 80%-20% and 60%-40% of relative proportions of cytoplasm and chloroplast (d) heterogenous spheres with 80%-18.63%-1.37% of relative proportions of cytoplasm, chloroplast and silica wall. A distinction is made between data corresponding to different diameters: $1 \leq d < 10 \mu\text{m}$ (grey dots), $10 \leq d < 20 \mu\text{m}$ (red dots), $20 \leq d \leq 40 \mu\text{m}$ (blue dots).

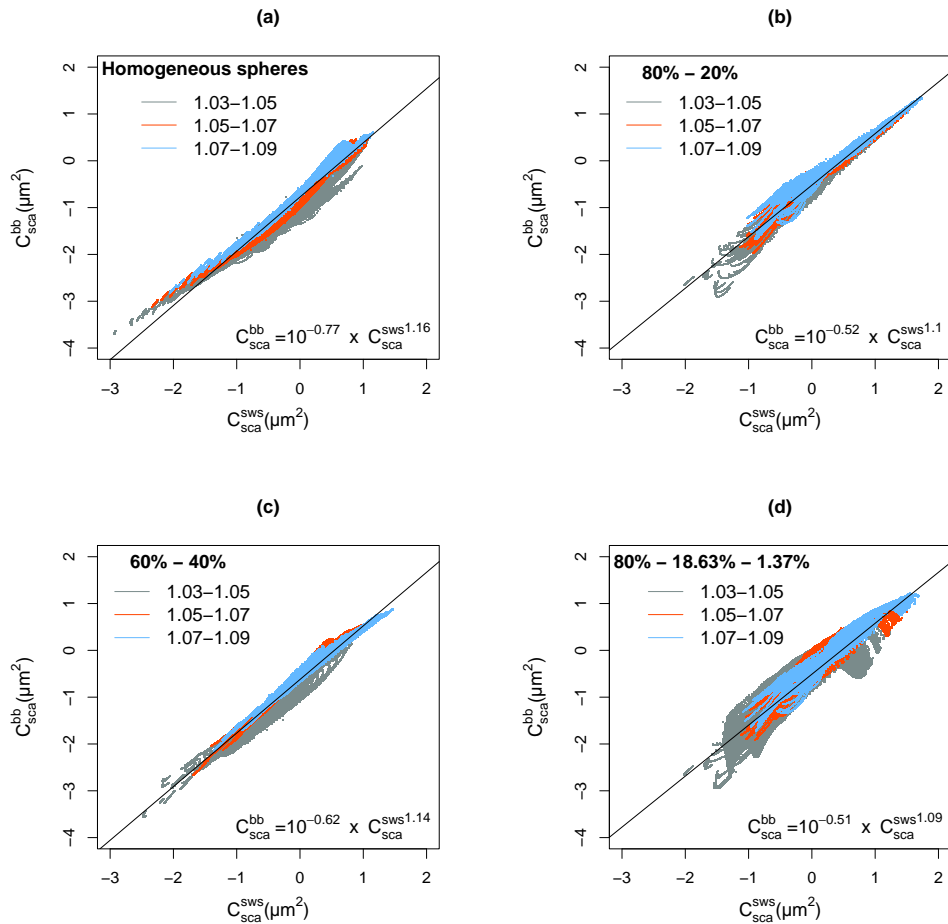


Fig. 6. Same as Fig. 5. A distinction is made between data corresponding to different volume equivalent refractive indices (real part): $1.03 \leq m_r \leq 1.05$ (grey dots); $1.05 < m_r \leq 1.07$ (red dots) and $1.07 < m_r \leq 1.09$ (blue dots).

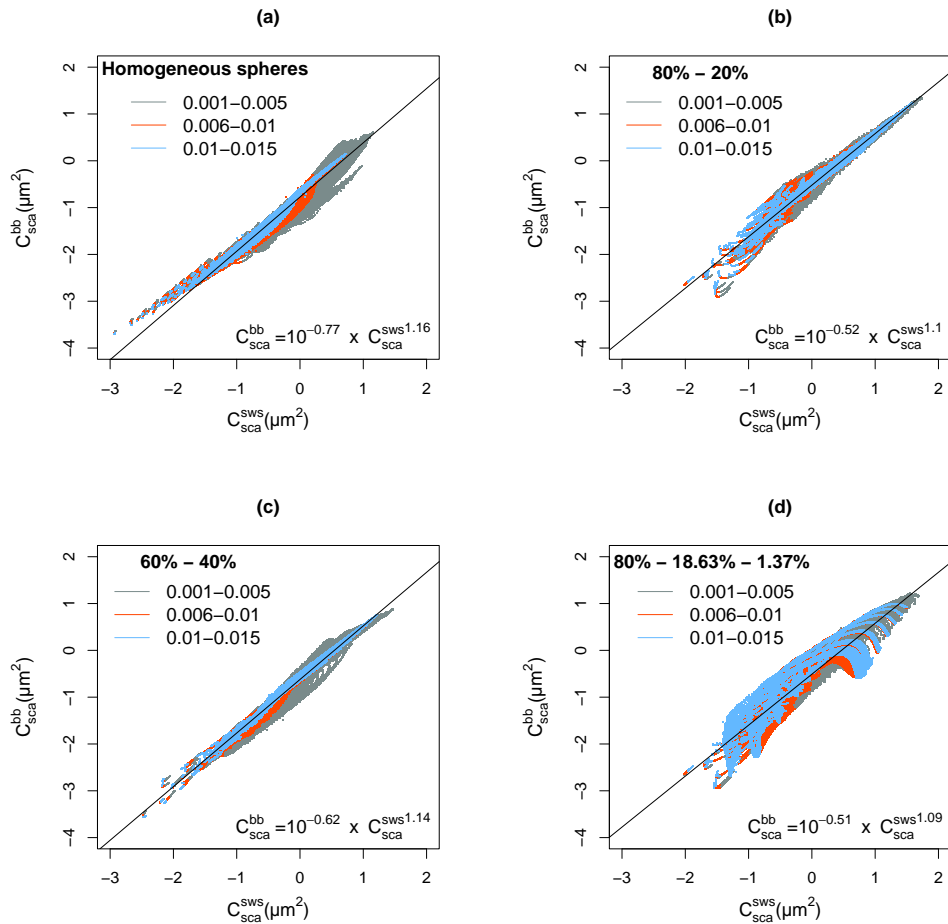


Fig. 7. Same as Fig. 5. A distinction is made between data corresponding to different different volume equivalent refractive indices (imaginary part) : $0.001 \leq m_i < 0.005$ (grey dots); $0.006 \leq m_i < 0.01$ (red dots) and $0.01 \leq m_i \leq 0.015$ (blue dots).

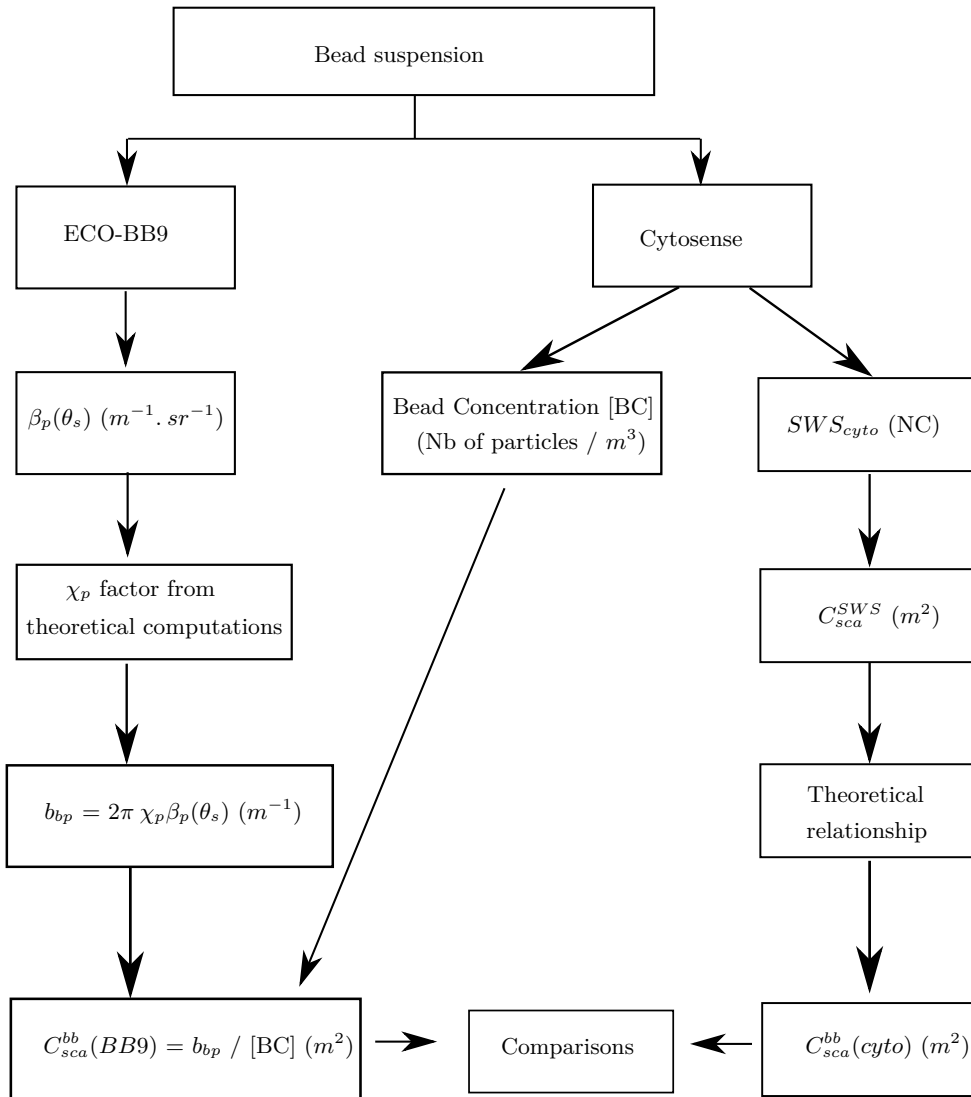


Fig. 8. Flowchart showing how CytoSense measurements and ECO-BB9 are converted into backscattering cross section to be compared

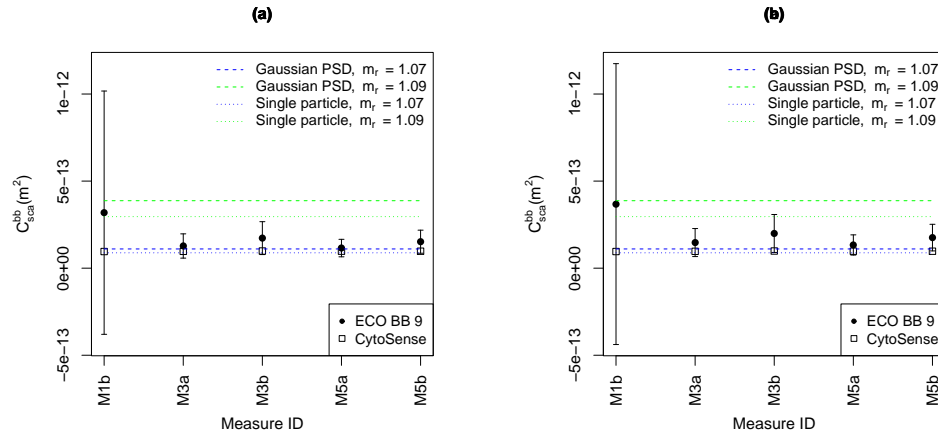


Fig. 9. Optical backscattering cross section of silica beads (5 μm in diameter) from ECO-BB9 (black dots), CytoSense (open squares) and Mie theory with $m_r = 1.07$ (blue lines), and 1.09 (green lines). Dotted and dashed lines correspond to simulations for perfect monodispersion and gaussian PSD with a CV of 30%, respectively. Error bars stand for the standard deviation over the mean C_{sca}^{bb} (BB9). Standard deviation over the mean C_{sca}^{bb} (cyto) are not represented as it is small compared to standard deviation over the BB9 cross section. ECO-BB9 signal was converted using (a) χ_p of 1.1 (b) χ_p of 1.27

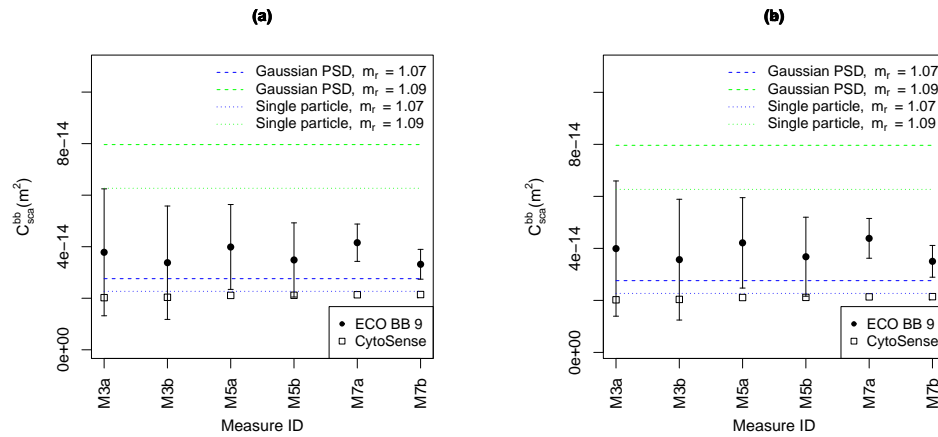


Fig. 10. Same as Fig. 9 but for 3 μm beads. ECO-BB9 signal was converted using (a) χ_p of 1.26 (b) χ_p of 1.33

7. Comparison

This section is dedicated to the comparison of the backscattering cross-section C_{sca}^{bb} as estimated from cytometric measurements and the backscattering coefficient of particles b_{bp} as measured by the WET Labs ECO-BB9 backscattering sensor (at 440, 488, 510, 530, 595, 650, 676, 715, 865 nm). The backscattering coefficient of particles is related to the backscattering coefficient cross-section C_{sca}^{bb} of a single particle using N/V the particulate concentration (particles per cubic meter) as shown in Eq. (7). Measurements of the VSF were conducted in a cylindrical polyethylene black tank (20.0 cm in diameter and 40.6 cm deep). The inside walls of the tank have a minimally reflective surface as they are black and flat. The tank was filled with 20 liters of Milli-Q water and measurements were performed to check for reflections in the tank. The instrument was handled vertically and lowered into the container until its face (with optical windows) was about 5 cm from the bottom. The instrument was then raised in steps and measurements were performed until no further changes in the raw signal, due to reflection on the walls of the tank, were observed. The backscattering remains constant when the instrument face is about 15 cm from the bottom. In this study, all measurements were realized with the instrument face immersed approximately 10 cm below the air-water interface (20 cm from the bottom of the tank). The experiment was conducted under dark conditions to prevent extraneous light entering the tank.

Comparisons between C_{sca}^{bb} (*cyto*) and C_{sca}^{bb} (BB9) were realized on dilutions of silica microspheres (Bangs Laboratories, Inc.) of 3 (L020503D-5412) and 5 (L100218C-9601) μm in diameter (Fig. 8). Beads were sonicated prior to use as recommended by the manufacturer. First, a steady clean-seawater baseline was measured to estimate the backscattering of pure water and if the Milli-Q water is contaminated, the backscattering of bacteria. The acquisition time was approximately 2 minutes with a sampling rate of 1Hz for the ECO-BB9 at 488 nm. The mean dark offset was calculated for each sensor over the corresponding time period. Then 1 or 2 ml of bead suspension were, several times, put into the tank to perform measurements on different bead concentrations. For each bead addition, the suspension was mixed up manually for approximately 3 minutes to obtain a homogeneous concentration. Measurements were performed with the ECO-BB9 and a water sample is taken for cytometric analysis. The raw signal was averaged over the acquisition time and the standard deviation was calculated. The mean signal was converted into $\beta_p(\theta_s)$ by first subtracting the mean dark offset, and then by multiplying the resulting value by the scaling factor as provided by WET Labs. Note that the last calibration of the instrument was realized December 18, 2013 and the experiment was conducted less than 4 months after this date (April, 2014). The ECO-BB9 single measurement $\beta_p(\theta_s)$ was converted into backscattering coefficient of particles as explained in section 4 using a χ_p factor. The ECO-BB9 measurements show a linear response of the backscattering signal to the bead addition (not shown here). It highlights that no tank effects and no multiple scattering occurred.

The χ_p factors, based on average phase functions from natural and poly-dispersed particle population, are not valid for monodispersions of beads. The phase function of a quasi monodispersed population is not smooth but exhibits a sequence of maxima and minima in the backward direction [22], contrary to the phase function for natural populations. The χ_p values for quasi monodispersed particles as reference bead were examined using Mie computations. As the real refractive index of silica beads is between 1.07 and 1.09 according to Bang Laboratories Inc., Mie computations were conducted for m_r of 1.07, 1.08 and 1.09. Mie computations were realized for silica beads modeling the particle size distribution (PSD) according to a Gaussian shape with a mean diameter of 3 or 5 μm and using a coefficient of variation (CV) of 30 %. The bead supplier indicated a coefficient of variation of 15% but measurements of bead diameters from scanning electron micrographs showed a higher coefficient of variation, around 30%. A non-negligible fraction of smaller or larger beads is observed. Larger beads are mainly

Table 2. Estimates from CytoSense - Silica beads of 3 μ m

Volume of the bead bead suspension (ml)	Sample ID	Number of particle $\times 10^{11}$ per m ³	Mean SWS $\times 10^{-12}$ (m ²)
3.0	M3a	1.3122	0.097
3.0	M3b	1.5010	0.097
5.0	M5a	4.5519	0.100
5.0	M5b	5.0954	0.100
7.0	M7a	7.2906	0.101
7.0	M7b	8.3442	0.0102

Table 3. Estimates from CytoSense - Silica beads of 5 μ m

Volume of the bead bead suspension (ml)	Sample ID	Number of particle $\times 10^{11}$ per m ³	Mean SWS $\times 10^{-12}$ (m ²)
1.0	M1a	0.0404	0.444
1.0	M1b	0.1735	0.434
3.0	M3a	1.1878	0.439
3.0	M3b	0.8768	0.446
5.0	M5a	2.1565	0.442
5.0	M5b	1.6367	0.442

due to two beads fused together. The angular weighting function of the ECO-BB9, $W_{bb}^{BB9}(\theta)$, is defined according to Sullivan et al., 2013 to account for the precise angular response of the sensor. Simulated values of $\beta_p(\theta)$ are multiplied by $W_{bb}^{BB9}(\theta)$ and then integrated over the field of view of the sensor to simulate the signal measured by the ECO-BB9 named $\beta_p(124^\circ)$ as the weighting function is centered around 124° .

The χ_p value is obtained according to Eq. (8) from the simulated values of $\beta_p(124^\circ)$ and b_{bp} . The χ_p factor increases with the refractive index and decreases with the particle size. It is due to the position of angular minima and extrema which slightly changes with size and refractive index. To convert $\beta_p(124^\circ)$ into b_b , two χ_p values are considered for a given diameter. For 3 μ m beads, a χ_p value, equal to 1.26 or 1.33, corresponds to m_r of 1.07 and 1.09, respectively. For 5 μ m beads, a χ_p equal to 1.10 and 1.27 corresponds to m_r of 1.07 and 1.09, respectively.

Cytometric measurements (abundance and sideward scattering) were realized twice on the same water sample to examine the reproducibility of the measurements, particularly in particle counting. Table 2 and 3 display the particle concentration and the mean SWS converted into C_{sca}^{SWS} as explained in Section 5. Samples are named M1, M3, M5 with 1,3, and 5 corresponding to the volume of bead suspension in the container (named V in the following) and with letters (a) or (b) distinguishing the duplicates.

The variability of particulate abundance is larger when the concentration of particles decreases. It is due to variability of particle counting CV_p , which follows a Poisson's law and is inversely proportional to \sqrt{n} , where n is the number of counted particles in a given sample volume per unit time. In addition to CV_p , the instrument variability (CV_c) has to be considered. The instrument variability (CV_c) is determined from repeated measurements (5-15 times) on the

same sample and is defined as the ratio of the mean abundance to the standard deviation. From analysis of 3 μm and 10 μm bead suspensions, Thyssen et al., 2008 showed that if the number of particles is large enough within the analyzed volume (>1000), the reproducibility of particle counting was achieved with $(CV_c + CV_p) < 3\%$. Comparisons of bead counts with a CytoSense (CytoBuoy b.v.), a Moflo (Dako) and a Cyturon (Cyturon Absolute ORTHO Diagnostic Systems) cytometer were performed by Thyssen et al., 2008. Results showed similar counts within the experimental uncertainties with no systematic bias for the CytoSense [39].

For a given bead size, the sideward cross section C_{sca}^{SWS} is relatively constant whatever the sample ID (Table 2 and 3). The mean C_{sca}^{SWS} is $0.0998\text{E-}12\text{ m}^2$ and $0.4413\text{E-}12\text{ m}^2$ for beads of 3 μm and 5 μm , respectively. These values are relatively close to values calculated from Mie theory ($0.082\text{E-}12\text{ m}^2$ and $0.367\text{E-}12\text{ m}^2$) for monodisperse silica beads considering m_r equal to 1.07 and no bead absorption.

The backscattering cross sections $C_{sca}^{bb}(BB9)$ derived from the ECO-BB9 at 488 nm are shown in Figs 9 and 10 and are compared with Mie computations. Error bars represent the associated standard deviations due to the instrumental variability of the ECO-BB9. Cytometric estimates were obtained by converting the measured C_{sca}^{SWS} into $C_{sca}^{bb}(cyto)$ using the theoretical relationship developed in Section 6 with the slope and the intercept calculated over the whole dataset ($A = 1.16$ and $B = -0.60$). For a given volume of bead suspension (1, 3, 5 or 7 ml), b_{bp} as measured by the ECO-BB9 leads to two values of $C_{sca}^{bb}(BB9)$ as it is divided by the particle abundance quantified from the (a) or (b) duplicates. Results corresponding to M1a sample are not displayed on Fig. 9 because the measured abundance was too low and hence unreliable.

For 5 μm beads, values of $C_{sca}^{bb}(BB9)$ at 488 nm range between $0.115\text{E-}12$ and $0.319\text{E-}12\text{ m}^2$ for χ_p of 1.10 (Fig. 9(a), black dots) and between $0.133\text{E-}12$ and $0.368\text{E-}12\text{ m}^2$ for χ_p of 1.27 (Fig. 9(b), black dots). For 3 μm beads, values of $C_{sca}^{bb}(BB9)$ are between $0.033\text{E-}12$ and $0.042\text{E-}12\text{ m}^2$ for χ_p of 1.26 (Fig. 10(a)) and between $0.035\text{E-}12$ and $0.044\text{E-}12\text{ m}^2$ for χ_p of 1.33 (Fig. 10(b)). Note that the variability of $C_{sca}^{bb}(BB9)$ is due to variability of particulate abundance as measured by the CytoSense. These values range between C_{sca}^{bb} values computed with Mie theory considering a Gaussian PSD and a CV of 30%. The mean value of $C_{sca}^{bb}(cyto)$ is $0.097\text{E-}12 \pm 0.0011\text{E-}12$ for 5 μm beads and $0.021\text{E-}12 \pm 0.0005\text{E-}12$ for 3 μm beads. Relative differences are defined as follows:

$$\Delta E (\%) = \frac{C_{sca}^{bb}(BB9) - C_{sca}^{bb}(cyto)}{C_{sca}^{bb}(BB9)}. \quad (19)$$

For 5 μm beads, relative differences between $C_{sca}^{bb}(cyto)$ and $C_{sca}^{bb}(BB9)$ range between 15% and 70% with a χ_p of 1.1 and between 27% and 74% for a χ_p of 1.27. Note that these differences are smaller than the instrumental variability. If M1b is not considered, the upper values of ΔE becomes 43% with a χ_p of 1.1 and 50% for a χ_p of 1.27. For 3 μm beads, relative differences ΔE are more important than the instrumental variability. They are between 35% and 48% with a χ_p of 1.26 and between 49% and 59% with a χ_p of 1.33.

The bead supplier indicates that an antibacterial agent is added in bead suspensions to avoid bacteria growth. Nevertheless, silica bead suspensions of 3 and 5 μm were examined using scanning electron microscopy to check the absence of such a particle background. No bacteria or other contaminating particles were detected from SEM micrographs. Consequently, discrepancies cannot be explained by a background particle contamination in bead suspensions. Differences between $C_{sca}^{bb}(cyto)$ and $C_{sca}^{bb}(BB9)$ can be partly explained by the impact of the particule size distribution on the measured signal. As the CytoSense measures the scattering of individual particles, its measurement is not influenced by the particle size distribution contrary to ECO-BB9 measurements. Mie computations show that C_{sca}^{bb} increases when a Gaussian PSD is considered and increases with the coefficient of variation. For example, considering 5 μm

beads and m_r of 1.07, C_{sca}^{bb} increases from 0.088E-12 for a perfect monodispersion to 0.110E-12 for a CV of 30%. For 3 μm beads, this values becomes 0.0230E-12 for a perfect monodispersion and 0.028E-12 for a CV of 30%. It implies that the minimum relative difference between CytoSense and ECO-BB9 measurements is around 20-25% and can not be attributed to uncertainties in calibrating the CytoSense, or inaccuracies introduced by the theoretical relationship used to convert C_{sca}^{SWS} into C_{sca}^{bb} . Such differences are due to the measured parameter itself which is the scattering of individual particles for CytoSense and the bulk scattering for ECO-BB9. Notice that, for 3 μm beads, the mean $C_{sca}^{bb}(\text{cyto})$ ($= 0.115\text{E-}12 \text{ m}^2$) is very close to the Mie value ($=0.110\text{E-}12 \text{ m}^2$).

Note that C_{sca}^{SWS} have been converted into C_{sca}^{bb} using the general relationship established from the 495,900 computations considering homogeneous and heterogeneous spheres. If we consider only computations corresponding to silica beads with m_i null, m_r of 1.07, 1.08 and 1.09, d between 1 and 40 μm (708 computations), the slope and the intercept are equal to 1.11 and -0.39, respectively. As these values are relatively close to A and B as previously calculated for the whole dataset, relative differences between CytoSense and VSF measurements are very close to previous ΔE values.

8. Concluding remarks

A very simple methodology has been developed to derive the backscattering cross section of individual particles from cytometric measurements. Possible sources of errors are firstly instrumental limitations and calibration errors or inaccuracies in the modelling of weighting functions. Comparisons were realized between CytoSense measurements and Mie theory on suspensions of polystyrene microspheres. Comparisons show mean absolute relative differences between 27.9% (FWS) and 41.8% (SWS). The larger relative differences have been observed on the sideward signal for large particles (above 20 μm in diameter) caused by light saturation of detectors which is more important for PMTs (sideward detectors) than for PIN photodiodes (forward detectors). For the LOG CytoSense less affected by the light saturation, the mean absolute relative differences are 33.7% (FWS) and 23.9% (SWS).

In a second step, a power law was used to convert the sideward cross section as measured by the CytoSense into the backscattering cross section. The scattering of data around the mean relationship, built from the whole dataset, introduces inaccuracies on backscattering estimates and constitutes a second source of errors. Particle diameter, refractive index (real and imaginary part) impacts the scattering of data, around the mean relationship and deviations from the mean relationship varies according the considered model (homogeneous spheres or heterogeneous spheres with two or three layers). More particularly, data points are more variable when the thickness of the outer layers is more important. Quantifying errors introduced by the use of a such mean relationship, is quite challenging as the structure and the refractive index of particles are unknown in the natural environment. Information on particle diameter could be obtained from the CytoSense measurements but cytometric estimates of particle diameter are, in some cases, inaccurate (for example diameter/length estimates from pulse shapes of small particles $< 5 \mu\text{m}$ become increasingly inaccurate with decreasing particle size).

To test the accuracy of the proposed methodology, a laboratory experiment was carried out on a suspension of silica beads to compare the backscattering cross section as measured by the ECO-BB9 backscattering sensor and the CytoSense flow cytometer. As the ECO-BB9 measures the VSF at one single angle, a conversion factor is required to derive the backscattering coefficient. As the χ_p factor defined by Sullivan et al., 2013 is valid only for natural polydispersed populations, a χ_p factor for quasi monodispersed silica beads was calculated using Mie computations. Comparisons showed relative differences of the same order of magnitude as instrumental variability. Relative differences can be quite large but they can partly be explained

by the fact that the CytoSense measures the cross section of individual particles, whereas the ECO-BB9 measures the bulk cross section.

The choice of bead suspensions instead of phytoplankton cultures was motivated by the fact that a population made up of spherical particles of known sizes can be more easily characterized. Scanning electron micrographs, realized in the framework of this study, did not show evidence for background particle contamination from submicron particle as bacteria in bead suspension. For phytoplankton cultures, the absence of non algal submicron particles as bacteria could not be guaranteed (even for axenic cultures) and submicron detritus also might have been present. In this case, direct comparison of bulk measurements and measurements on individual particles will be less obvious. Differences between the backscattering cross section as estimated by the ECO-BB9 and the CytoSense could be attributed to a “bulk effect” instead of inaccuracies coming from the proposed methodology. In future studies, it could be helpful to identify separately the impact of submicron particles as bacteria, which can impact greatly the bulk backscattering. A possible method is to perform measurements of bulk backscattering before and after filtration. Another option would be to use a CytoSense with high sensitivity performance (the trigger level of 16 mV on side scatter might be low enough to detect certain submicron particles or larger bacteria) or a dedicated cytometer to measure the bacterial abundance. Then, the bacterial backscattering cross section could be simulated from the bacterial abundance using Mie theory and the backscattering signal could be estimated by adding the bacterial contribution to the contribution of phytoplankton cells and non-living particles.

In phytoplankton cultures, particles can be non-spherical. For oriented non-spherical particles, the signal measured by CytoSense can depend on the first element of the scattering matrix Z_{11} but also on the element Z_{13} . Indeed, the scattering matrix (and so the phase matrix) becomes a function of the zenith and azimuth angles of the incident and scattered radiation and the Z_{13} element is not null. In this case, the CytoSense signal cannot be converted in terms of backscattering coefficient and comparisons with the ECO-BB9 signal are not valid. However, first radiative transfer simulations with the T-matrix code dedicated to non spherical particles in a fixed orientation [40], show that for small oriented spheroids with a weak aspect ratio, Z_{13} is negligible and particles can be considered as spherical. Consequently, the proposed methodology will be still valid. These results should be confirmed with a large database of study cases, including also computations for spheroids with a large aspect ratio and also computations of the T-matrix code dedicated to externally aggregated multi-sphere clusters in fixed orientations [41]. Note that, even if the theoretical relationship is not valid for oriented particles/aggregates with a high aspect ratio, the sideward scattering as measured by CytoSense can be still used in addition with measurements of backscattering sensors.

Acknowledgments

The authors gratefully acknowledge the support from the French Space Agency (CNES) through the TROPHY project (CNES/TOSCA program). The authors thank Prof. Alexander Cunningham (University of Strathclyde, Scotland) and Dominic Stuart (CytoBuoy, b.v., NL) for the precious advices. Thanks to Laurent Brutier (LOG/ULCO) for his technical help. We appreciate thoughtful comments from two reviewers, which helped to improve this manuscript.